

# Mapping the Local Bubble’s Magnetic Field in 3D

Theo O’Neill<sup>1,2</sup>, Alyssa Goodman<sup>1</sup>, Juan Soler<sup>3</sup>, Jiwon Jesse Han<sup>1</sup>, and Catherine Zucker<sup>3</sup>

<sup>1</sup>Harvard-Smithsonian Center for Astrophysics (CFA)

<sup>2</sup>University of Virginia

<sup>3</sup>Affiliation not available

January 11, 2023

## Abstract

We present a 3D map of magnetic field orientation on the surface of the Local Bubble. This map is the first of its kind to fully chart magnetic fields over an observed superbubble. Recent work mapping the 3D shape and dynamics of the Local Bubble has revealed that the formation of all young stars within 200 pc of the Sun was triggered by the Bubble’s rapid expansion. The exact mechanics of this expansion, and the role that magnetic fields in the surrounding interstellar medium have played in regulating its evolution, is not yet clear. By combining detailed models of the Bubble’s geometry (derived from 3D dust mapping) with the assumption that magnetic field vectors are tangent to the Bubble’s surface, we are able to infer the 3D magnetic field orientation from Planck plane-of-the-sky dust polarization orientations. We analyze the relationship between the Bubble’s inferred magnetic field and background starlight polarimetry observations, and discuss how magnetic fields may have affected the dynamics of the Local Bubble and other nearby structures in the ISM.

## Introduction

Star formation is typically clustered, so expanding, low-density superbubbles  $\sim 100$ s of parsecs in diameter generated by sequential supernovae are common throughout the interstellar medium (ISM), both in the Milky Way (missing citation) and beyond (missing citation); (missing citation); (missing citation). These superbubbles are expected to play a significant role in concentrating and distributing the effects of stellar feedback (missing citation); (missing citation) and in triggering the formation of dense gas and stars (missing citation); (missing citation).

Numerical and hydrodynamical simulations predict that magnetic field orientation has a significant impact on the direction of superbubble expansion (missing citation); (missing citation), but the overall role of magnetic fields in regulating the formation, expansion, and effects of superbubbles is unclear. It has recently become possible to map the 3D magnetic field structure of individual molecular clouds within superbubbles (missing citation); (missing citation), but while 2D measurements of magnetic field strength over entire superbubbles have been obtained (missing citation); (missing citation); (missing citation); (missing citation); (missing citation), efforts to map the 3D orientations of magnetic fields over the entire surfaces of superbubbles have been limited by uncertainties on their 3D geometries.

The Local Bubble is an an expanding, low-density superbubble centered roughly near the Sun’s present day location. Due to its proximity and well-studied nature, the Local Bubble is an ideal candidate to map magnetic field structures in 3D across a superbubble’s surface for the first time. The Local Bubble was

likely generated by a series of supernovae within the last 15 Myr and is surrounded by a thin, irregular shell of cold dust and gas extending up to a few hundred parsecs from the Sun (missing citation); (missing citation); (missing citation); (missing citation). Recent work mapping the 3D geometry of the Local Bubble (missing citation) has enabled detailed analysis of its relationship to molecular clouds and star-forming regions adjacent to its surface, and suggested that nearly all local star formation within 200 pc of the Sun was triggered by the Bubble’s expansion (missing citation).

However, the exact mechanics driving the Local Bubble’s formation and expansion are not yet entirely clear. Additionally, information on how magnetic fields may effect the bubble’s dynamics and evolution, and by extension local star formation, is limited. B-field orientations inferred from polarization measurements are generally oriented parallel to the Galactic plane, but the B-field in the local ISM has been observed to depart from this ordered behavior (missing citation); (missing citation); (missing citation). Studies of the Local Bubble have suggested that it could be responsible for the nearby variations from this trend. An accurate 3D map of the Local Bubble’s magnetic field structure would then not only be a useful probe of the nearby history of star formation and general relationship between superbubbles, but also serve to constrain the variations between the local and larger-scale Galactic magnetic fields.

(missing citation) modeled magnetic fields on the surface of the Local Bubble at high latitudes ( $|b| > 60^\circ$ ) with the simplifying assumption that the shell has an ellipsoidal geometry, and concluded that variations in the B-field in these polar regions would be sufficient to distort measurements of Galactic field by a significant amount. (missing citation) and (missing citation) extended this work with a more physically motivated geometry enabled by 3D dust mapping of the Local Bubble’s surface by (missing citation), and reached similar conclusions that the Local Bubble’s surface makes a large contribution to the total observed sub-mm dust polarization at high latitudes. (missing citation) studied magnetic field strength and grain alignment on the Local Bubble’s surface using archival optical polarimetry observations, and found that the strength of the Bubble’s magnetic field as well as grain alignment efficiency varies significantly across its surface.

In this work, we create a three-dimensional map of the Local Bubble’s magnetic field structure. Specifically, we constrain the Local Bubble’s magnetic field structure by combining its known surface geometry with *Planck* polarization observations and background starlight polarization measurements. We assume that the magnetic field’s inclination is tangent to the surface of the Local Bubble (missing citation), and that the observed plane-of-sky magnetic field is primarily generated by a polarizing layer on the surface of the Local Bubble. Combining these assumptions with polarization observations constraining the plane-of-sky field orientations results in a complete set of 3D B-field vector orientations. This enables a full characterization of the B-field orientation over the surface to create the first-ever 3D map of a magnetic field over a superbubble.

In § we describe the data used in our analysis. We describe the construction of the 3D magnetic field map from *Planck* dust polarization data in §, and discuss the association between the field and the Local Bubble’s surface and local environment in §. We compare the *Planck*-derived magnetic field to background starlight polarization measurements in § before concluding in §.

## Observations

We summarize the construction of the 3D model of the LB’s inner surface created by (missing citation) in §. In §, we describe the Planck dust polarization map used to infer B-field orientation over the surface of the LB. We describe the background starlight polarimetry catalog against which we compare our inferred LB surface B-field in §.

## Dust-based Map of the Local Bubble

(missing citation) created a 3D map of the LB’s surface through analyzing the 3D dust reddening map created by (missing citation) from Gaia DR2 and 2MASS photometry and astrometry. They identified inflection points along the curves of the differential extinction as a function of distance from the Sun as marking the inner and outer edges of the LB’s shell. P20’s model is derived from these inner inflection points, with distances from the Sun to the surface ranging from 80 – 310 pc and a median distance of 215 pc. Uncertainties on distances and the shape of the LB are largest near the North and South poles, as it is unclear if the LB is a closed surface or is closer to a “chimney” structure with openings in the directions of the Galactic Halo (missing citation); (missing citation); (missing citation). The full model is shown in 3D in Figure 1a.

We reconstructed a continuous surface from the P20 map using `PyVista`, a Python interface for the Visualization Toolkit (VTK). As described by (missing citation) and automated in VTK, this process first builds a local connectivity graph between the full set of P20 points and fits tangent planes to the immediate neighborhood of each P20 point. It then computes a signed distance metric between evenly points spaced over a 3D grid and the corresponding closest tangent planes. The reconstructed surface is defined as the contour of this grid of signed distances at zero, and is shown in Figure 1b.

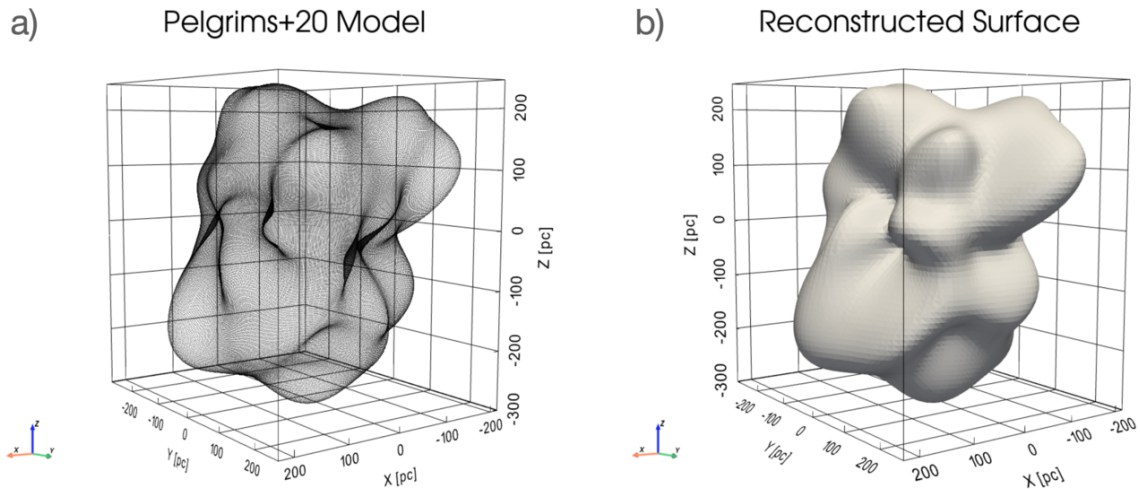


Figure 1: a): The 3D model of the Local Bubble’s inner surface created by P20 is shown by the black scatter points. b): Continuous surface of the LB reconstructed from a) is shown by the solid white volume.

## Planck Polarization Observations

To constrain the polarization in the dusty shell of the LB, we use the component-separated version of the 353 GHz Stokes  $I$ ,  $Q$ , and  $U$  maps released as part of the 2018 Planck data release (missing citation)<sup>1</sup>, produced using the Generalized Needlet Internal Linear Combination (GNILC) algorithm (missing citation). The GNILC algorithm was designed to separate foreground Galactic polarized thermal dust emission from polarized CMB emission (missing citation), making this public map appropriate for our study of nearby ( $d \lesssim 500$  pc) polarization. Using the Python package `healpy` (missing citation), we then smoothed the maps using a Gaussian beam with  $\sigma = 2^\circ$  to achieve uniform signal to noise resolution across the field.

<sup>1</sup>[COM\\_CompMap\\_IQU-thermaldust-gnilc-unires\\_2048\\_R3.00](https://www.cosmos.esa.int/documents/10180/1365231/COM_CompMap_IQU-thermaldust-gnilc-unires_2048_R3.00)

We calculate polarized intensity  $P$  as  $P = \sqrt{Q^2 + U^2}$  and polarization fraction as  $p = P/I$ . Polarization angle  $\phi$  is defined as

$$\phi = \frac{1}{2} \arctan(-U, Q), \quad (1)$$

and is measured from the northern Galactic pole according to IAU conventions, with positive values increasing with increasing Galactic latitude  $\ell$  (missing citation). The long axis of dust grains, and resulting polarization vectors, are typically perpendicular to the plane-of-the-sky component of  $B$ , so we assume that  $\phi$  is perpendicular to the plane-of-sky B-field orientation  $\Psi_{\perp}$  ( $\Psi_{\perp} = \phi + \frac{\pi}{2}$ ). Our goal is to infer the 3D B-field orientation  $\Psi$ , which will by construction appear identical to  $\Psi_{\perp}$  when viewed in 2D  $\ell$ - $b$  projection.

## Starlight Polarization Measurements

Dust polarization measurements yield the plane-of-sky orientation of magnetic fields averaged over an entire line of sight. We supplement this information with background starlight polarimetry observations, which are able to probe much smaller angular scales than dust alone and can also constrain polarization as a function of distance.

(missing citation) assembled a catalog of starlight polarization measurements for stars within 500 pc of the Sun (measured with Gaia DR2 distances), which includes a subset of nearby stars in the earlier catalog of (missing citation). Following (missing citation), we only use measurements with a ratio of polarization degree to uncertainty of  $P/\sigma(P) \geq 3$ , yielding a total sample of  $\sim 4150$  stars. Since the short axis of dust grains is typically aligned parallel to the surrounding magnetic field, starlight observations yield polarization angles  $\phi_{\star}$  parallel to the plane-of-sky component of the B-field,  $\phi_{\star} = \Psi_{\star}$ .

## Construction of 3D Magnetic Field

We calculated the 3D magnetic field orientation  $\Psi$  under the assumption that the magnetic field's inclination is tangent to the surface of the LB.

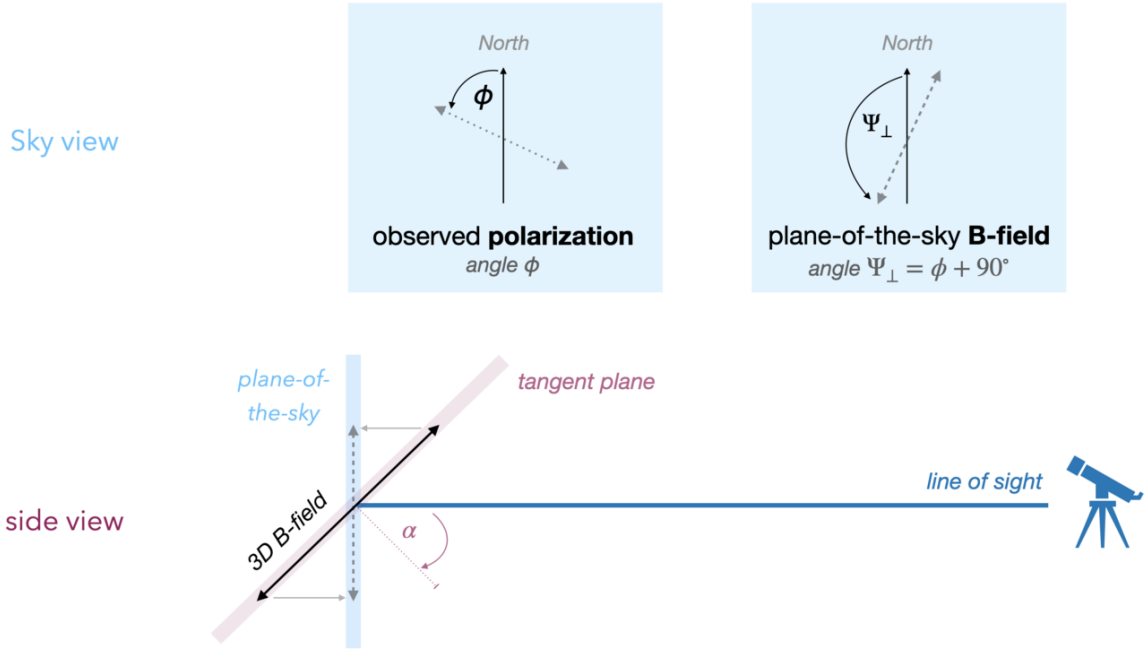


Figure 2: Assuming a magnetic field confined to the Bubble’s tangent plane (pink), the “true” 3D magnetic field orientation is given by the 3D vector (solid black) “in the tangent plane”. That vector projects to the 2D vector (dashed gray) seen on the plane-of-the-sky (blue).

For each point on the bubble’s surface in the P20 map, we fit a plane to its 50 nearest neighbors in 3D space. This set of nearest points typically spanned a space between 6–8 pc in radius. We then performed a nearest neighbors search between the P20 points (projected to 2D Galactic coordinates) and the Planck measurements through constructing a ball tree. Separations within the tree were calculated using the Haversine distance metric, which assesses the angular separation between points on a sphere. The separation between a given LB surface point and its nearest Planck point was on average  $<0.01^{\circ}$ .

We projected the nearest Planck pseudovector  $\vec{\Psi}_{\perp}$  to Cartesian coordinates and defined a plane along the line of sight between the Sun and the projected vector. We then defined a unit vector  $\vec{\Psi}$  along the intersection of the line-of-sight plane with the surface’s tangent plane. This vector represents our inferred 3D B-field orientation on the surface of the LB. For an observer at the Sun, this new vector would appear identical to the plane-of-sky  $\vec{\Psi}_{\perp}$ ; however, its 3D orientation is informed by the geometry of the LB.

We selected a subsample of the full set of derived  $\vec{\Psi}$  evenly spaced at  $\sim 10$  pc intervals. The resulting 3D vector field is shown over the reconstructed LB surface in Figure 3. We also generated streamlines representing the B-field through integrating the full vector field over the surface with a Runge-Kutta-Fehlberg integrator, as implemented in `PyVista`. Since we have no information about the direction of the magnetic field at any given point on the surface, only its orientation, we integrate both “upstream” and “downstream”. This integrated field is also shown in Figure 3 and is a 3D analog of the 2D LIC representation.

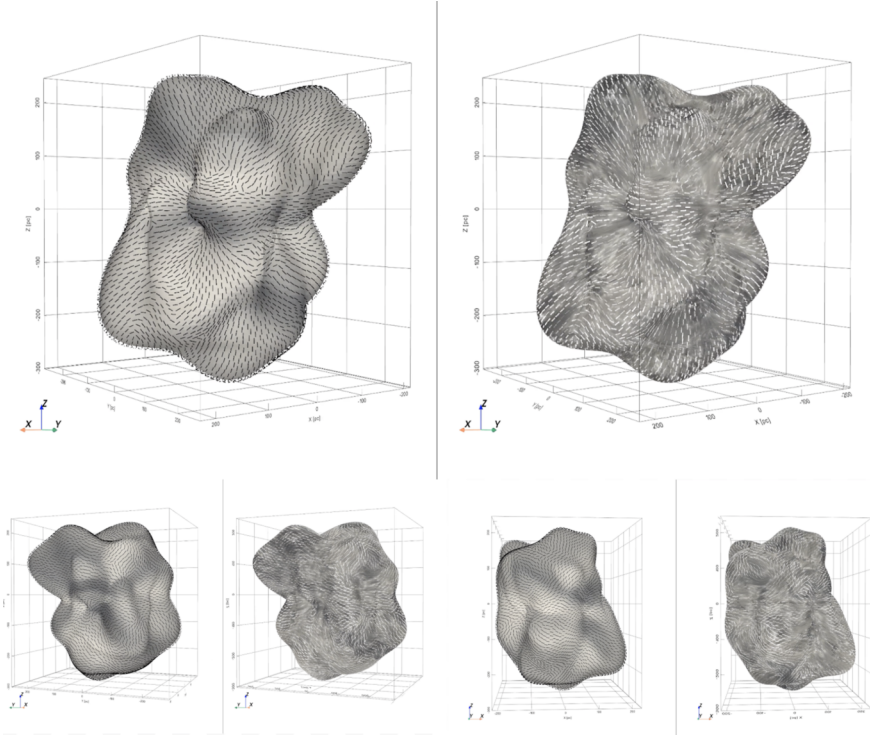


Figure 3: 3D views of magnetic field orientation over the surface of the Local Bubble. For each pair of views of the LB, left panel shows a vector field representation and right panel shows streamlines.

Rich media available at <https://www.youtube.com/watch?v=R09UrAXIwcQ>

## Comparison of 3D Field to Surface Features and Environment

The derived 3D B-field appears topologically correlated with features on and around the Local Bubble’s surface. In this section, we examine associations between LB and its environment.

### Comparison to Environment

Figures 4 and 5 give an overview of nearby structures in the ISM that surround the Local Bubble in 2D and 3D. An interactive 3D figure is also available<sup>2</sup>.

<sup>2</sup>[https://faun.rc.fas.harvard.edu/czucker/Paper\\_Figures/Local\\_Bubble\\_Magnetic\\_Field.html](https://faun.rc.fas.harvard.edu/czucker/Paper_Figures/Local_Bubble_Magnetic_Field.html)

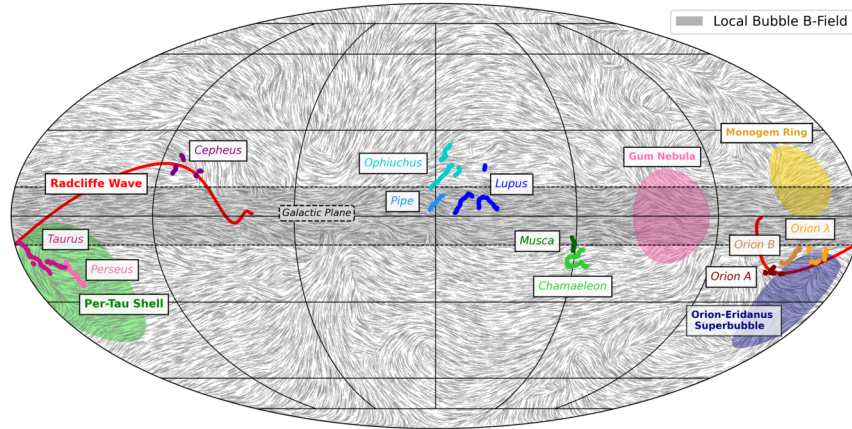


Figure 4: Overview of structures surrounding the LB, projected into 2D.

Rich media available at <https://youtu.be/hnGMF7Wafjo>

Table A1 summarizes the 2D and 3D data sources used to populate the LB’s environment. References include: (missing citation), (missing citation).

**Table A1.** 3D Structures in Interactive Figure

| Object Type              | Name  | Notes   | Reference  |
|--------------------------|---|---|--|
| <b>Dust</b>              | Dust Map  | $n_H \sim 10 \text{ cm}^{-3}$   | <a href="#">Leike et al. (2020)</a>  |
| <b>Local Bubble</b>      | Local Bubble Model<br>Magnetic Field Model                    | —<br>—  | <a href="#">Pelgrims et al. (2020)</a><br>This work  |
| <b>Molecular Clouds</b>  | Skeletons   | Cepheus, Chamaeleon, Corona Australis, Lupus,<br>Musca, Ophiuchus, Orion, Perseus, Pipe, Taurus   | <a href="#">Zucker et al. (2021)</a>   |
| <b>Larger Structures</b> | Radcliffe Wave<br>Split<br>Northern Celestial Pole Loop       | —<br>—<br>Prolate Spheroid  | <a href="#">Alves et al. (2020)</a><br><a href="#">Lallement et al. (2019)</a><br><a href="#">Marchal &amp; Martin (2022)</a>                                    |
| <b>Shells (3D)</b>       | Per-Tau Shell<br>Orion Shell<br>OBP-B1<br>Cepheus Flare Shell | $(x, y, z, R) = (-190, 65, -84, 78) \text{ pc}$<br>Ellipsoidal<br>$(x, y, z, R) = (-312, -130, -105, 33) \text{ pc}$<br>$(x, y, z, R) = (-156, 249, 79, 50) \text{ pc}$                                   | <a href="#">Bialy et al. (2021)</a><br><a href="#">Foley et al. (2022)</a><br><a href="#">Foley et al. (2022)</a><br><a href="#">Dharmawardena et al. (2022)</a> |
| <b>Shells (2D → 3D)</b>  | Gum Nebula<br>Vela SNR<br>Monogem Ring                        | $(l, b, d, D) = (258^\circ, -2^\circ, 400 \text{ pc}, 36^\circ)$<br>$(l, b, d, D) = (264^\circ, -3.4^\circ, 290 \text{ pc}, 8^\circ)$<br>$(l, b, d, D) = (203^\circ, 12^\circ, 300 \text{ pc}, 25^\circ)$ | <a href="#">Sushch et al. (2011)</a><br><a href="#">Sushch et al. (2011)</a><br><a href="#">Knies et al. (2018)</a>  |

## Comparison to Surface Features

Figure 6 compares a 2D projection of distance to the LB’s surface with the orientation of the plane-of-sky magnetic field  $\Psi_\perp$ . There appears to be strong correlations between local field orientation and distance to the Bubble’s surface, suggesting a topological relationship between the two.

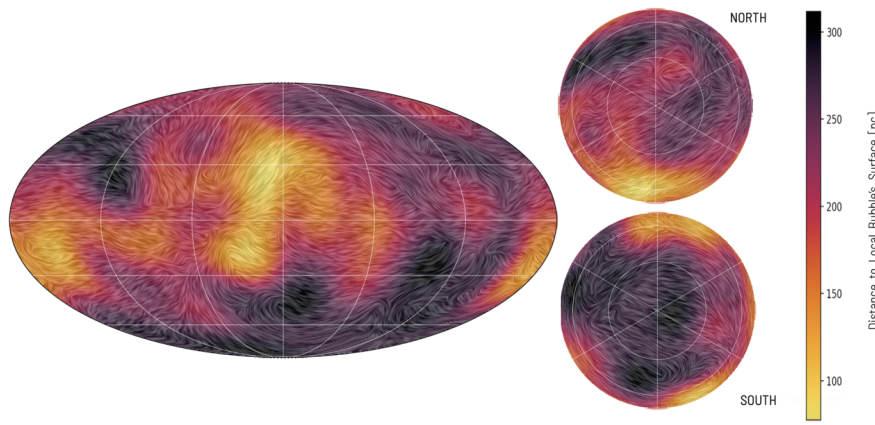


Figure 5: Left: Mollweide projection of distance to the surface of the LB in the P20 map, with an overlaid drapery pattern produced through Line Integral Convolution showing the orientation of the plane-of-sky magnetic field. Right: As above, but for polar projections centered on North (top) and South (bottom) Galactic poles.

We calculated the mean curvature at each point on our reconstructed LB surface using PyVista, with results shown in Figure 7 in both 2D and 3D. When projected to 2D and compared to the plane-of-sky  $\Psi_{\perp}$ , there appear to be clear associations between highly curved surface points and distortions or changes in the field orientation.

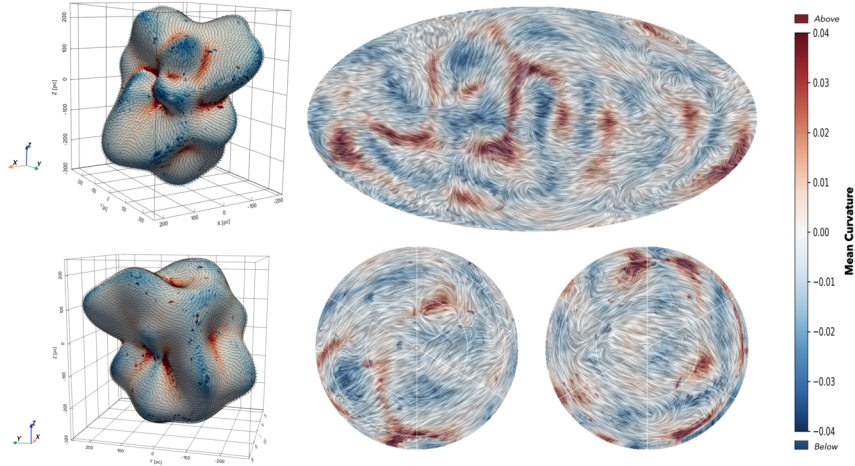


Figure 6: Left: Mean curvature of the LB's surface is shown in 3D. Right: As left, but in 2D Mollweide projection (top), and for polar projections centered on North (bottom left) and South (bottom right) Galactic poles. The LIC representation of plane-of-sky magnetic field is overlaid.

Rich media available at <https://www.youtube.com/watch?v=j0RA-lWqE04>

Similar trends hold for the angle between the Local Bubble's tangent plane and the plane of the sky  $\alpha$  at each point on the LB's surface, as shown in Fig 8.

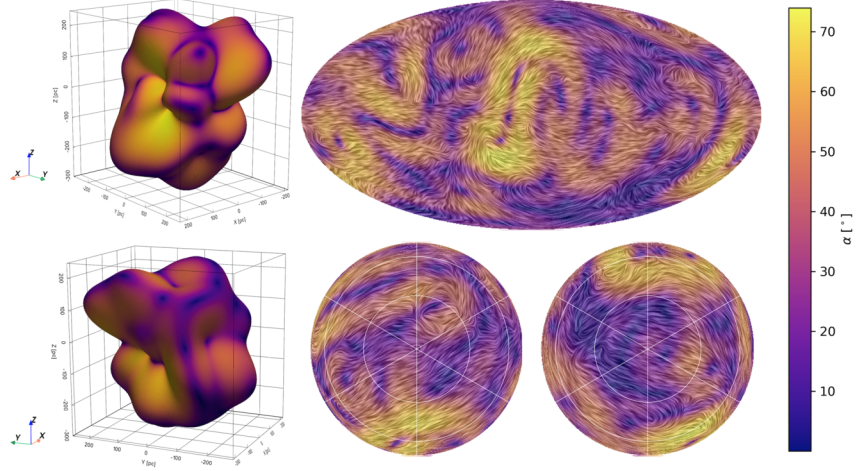


Figure 7: As Figure 7, but with angle between the Local Bubble surface and the plane of the sky.

## Dispersion and Spatial Autocorrelation

We calculated the dispersion in the plane-of-sky B-field at each point on the 3D surface as (missing citation)

$$\varsigma_{\Psi_{\perp}} = \left( \frac{1}{N-1} \sum_{i=1}^N (\bar{\Psi}_{\perp} - \Psi_{\perp}^{(i)})^2 \right)^{1/2}, \quad (2)$$

where  $\bar{\Psi}_{\perp}$  is the average  $\Psi_{\perp}$  inferred for the  $N = 10$  nearest points.  $(\bar{\Psi}_{\perp} - \Psi_{\perp}^{(i)})$  is defined as

$$\bar{\psi}_{\perp} - \psi_{\perp}^{(i)} = \frac{1}{2} \arctan \left( q^{(i)} \bar{u} - \bar{q} u^{(i)}, q^{(i)} \bar{q} + u^{(i)} \bar{u} \right), \quad (3)$$

where  $q$  and  $u$  are the reduced Stokes parameters  $q = Q/I$  and  $u = U/I$ . The derived dispersions are shown in 2D and projected back to 3D in Figure 9. High dispersion surface points tend to follow distinct curves over the surface, most notably near the projected locations of Orion, Cepheus, and Perseus/Taurus.

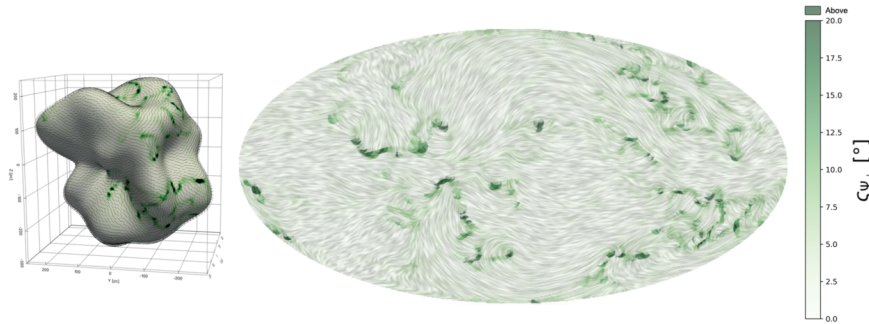


Figure 8: Left: Dispersion of the plane-of-sky B-field is shown. Right: As left, but in 2D Mollweide projection with LIC-representation overlaid.

Rich media available at <https://youtu.be/XQxDeAYZc1E>

We next assess spatial autocorrelation in our vector field. We extend the work of (missing citation) to calculate Moran’s I statistic for “directionless” vectors (where upstream or downstream motion along a given vector orientation is indistinguishable).

We define a local Moran’s  $I_i$ ,

$$I_i = \frac{|\vec{m}_i \cdot \vec{\bar{m}}|}{S_i^2} \sum_j w_{ij} |\vec{m}_j \cdot \vec{\bar{m}}|, \quad (4)$$

where

$$\vec{m}_i = (B_{li}, B_{bi}), \quad (5)$$

$$\vec{\bar{m}} = \left( \frac{\sum_i B_{li}}{n}, \frac{\sum_i B_{bi}}{n} \right) = (\bar{B}_l, \bar{B}_b). \quad (6)$$

Calculating the absolute value of dot product ensures that pseudovectors that appear to point in the same direction ( $\vec{m}_i \cdot \vec{m}_j \simeq 1$ ) are treated the same as pseudovectors that appear to point in opposite direction ( $\vec{m}_i \cdot \vec{m}_j \simeq -1$ ); this is required since we can only define the orientation but not direction of our 3D magnetic field.

We define weights as the inverse of the distance between 2D points projected to a 3D sphere ( $w_{ij} = 1/d_{ij}$ ) and variance  $S_i^2$  as

$$S_i^2 = \frac{\sum_{j=1, j \neq i} (|\vec{m}_i \cdot \vec{m}_j|)^2}{(n-1)}. \quad (7)$$

The expectation value of  $I_i$  under the null hypothesis (no spatial association) is

$$E[I_i] = -\frac{\sum_j w_{ij}}{n-1}. \quad (8)$$

We calculate  $I_i$  and  $E[I_i]$  for each point in our map, and report a normalized local Moran’s I statistic,

$$\sigma_{I_i} = \frac{I_i - E[I_i]}{\delta} \quad (9)$$

where  $\delta$  is the standard deviation of the full distribution of all  $I_i$ . Higher  $\sigma_{I_i}$  indicate higher degrees of spatial autocorrelation. The spatial distribution of  $\sigma_{I_i}$  is shown in Figure 10. Spatial autocorrelation closely follows 2D dispersion and appears associated with 3D features; future analysis will quantify this potential effect.

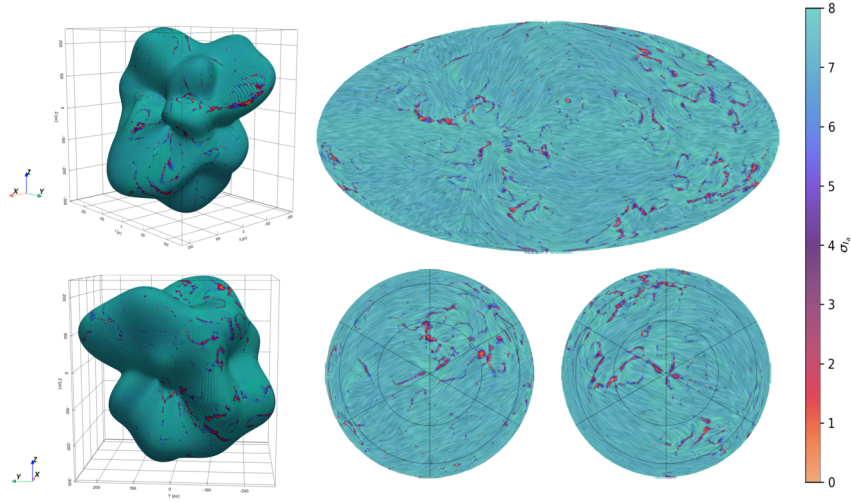


Figure 9: As Fig. 7, but for normalized local Moran’s I statistic.

Rich media available at <https://www.youtube.com/watch?v=igzxZrMV0jE>

## Confidence in Map Assumptions

Using the python package `dustmaps` (missing citation), we integrated the (missing citation) 3D dust map (with maximum distances ranging from  $\sim 270$  pc – 570 pc from the Sun) along each line of sight included in our 2D B-field map at 1 pc distance intervals. For each line of sight, this yielded a total  $\Sigma\tau_G/(1\text{pc})$ , which we converted to  $A_G$  as  $A_G = 1.086\tau_G$  and then  $A_V = 1.256A_G$  (missing citation). We repeated this exercise for the 2D foreground Planck extinction map included by `dustmaps`, calculating  $A_V$  as  $A_V = 3.1E(B - V)$ .

Figure 11 shows the ratio of the integrated Leike to Planck extinctions. We find that, for the majority of the sky, integrated local dust extinction is  $\geq 1/2$  the extinction measured by Planck (with the exception of the Galactic plane). This suggests that our 3D B-field map, which is built on the assumption that local dust is the dominant source of on-sky polarization, is most reasonable in these regions. In the interactive figure accompanying this paper, we mark B-field vectors that have an extinction ratio  $< 1/2$  (i.e., are less reliable) with thinner vectors.

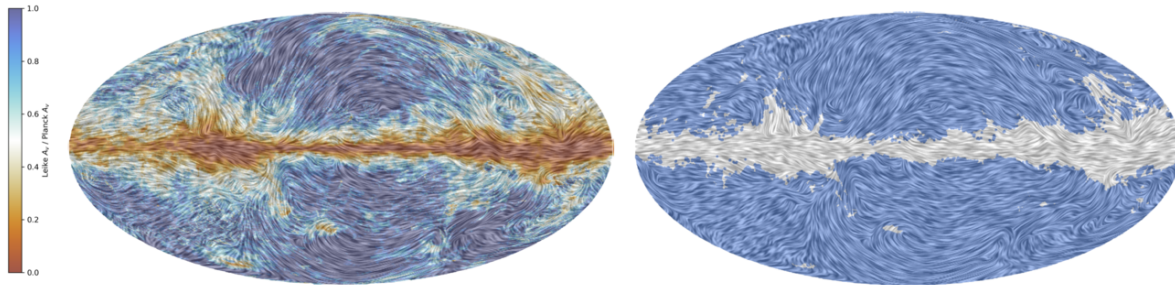


Figure 10: Left: Ratio of integrated Leike extinction  $A_v$  to Planck extinction. LIC map of B-field overlaid. Right: Regions on the left that have a ratio  $\geq 0.5$  are colored in blue.

## Comparison to Starlight Polarization

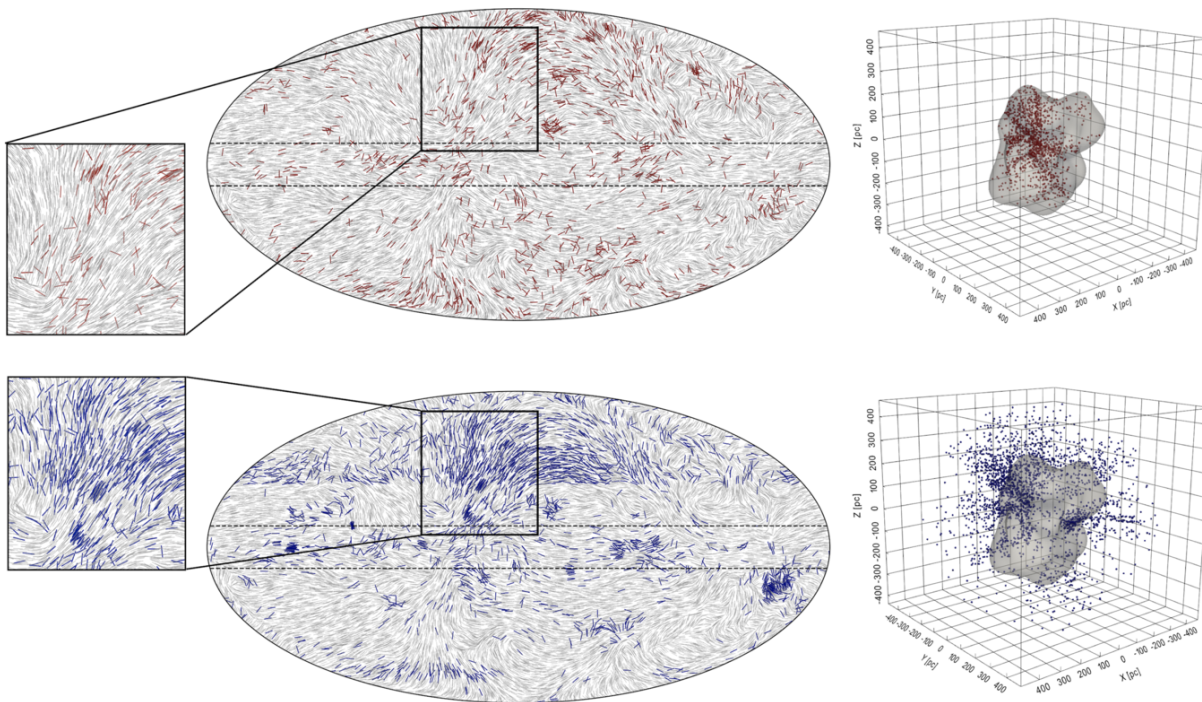


Figure 11: Starlight polarization and position relative to the Local Bubble surface. Top row: stars inside the Local Bubble, shown in red. Vectors mark the orientation of the inferred magnetic field at star positions in 2D Galactic projection (center), with the magnetic field derived for the LB surface shown by the gray vector field. Points indicate star positions in Cartesian space (right). A conservative vertical extent of the Galactic Plane is shown by the horizontal black dashed lines, inside of which we expect our assumption that the dominant polarization source along the line of sight is the LB to be less accurate. A magnified view of one 2D region is shown (left). Bottom row: As above, but for stars outside the Local Bubble, shown in blue.

We supplement the information about the LB's 3D B-field derived from the Planck observations with nearby starlight polarization observations. The interior of the LB has been observed to be a very low polarization region, in contrast to a more significant degree of polarization outside of the Bubble. (missing citation) observed a steep jump in polarization degree  $P$  at a distance of  $\sim 100$  pc from the Sun, which they suggested was the result of the transition from the interior to exterior of the LB. The recent (missing citation) 3D model allows us to identify at high resolution which stars in the (missing citation) sample fall inside vs. outside of the LB.

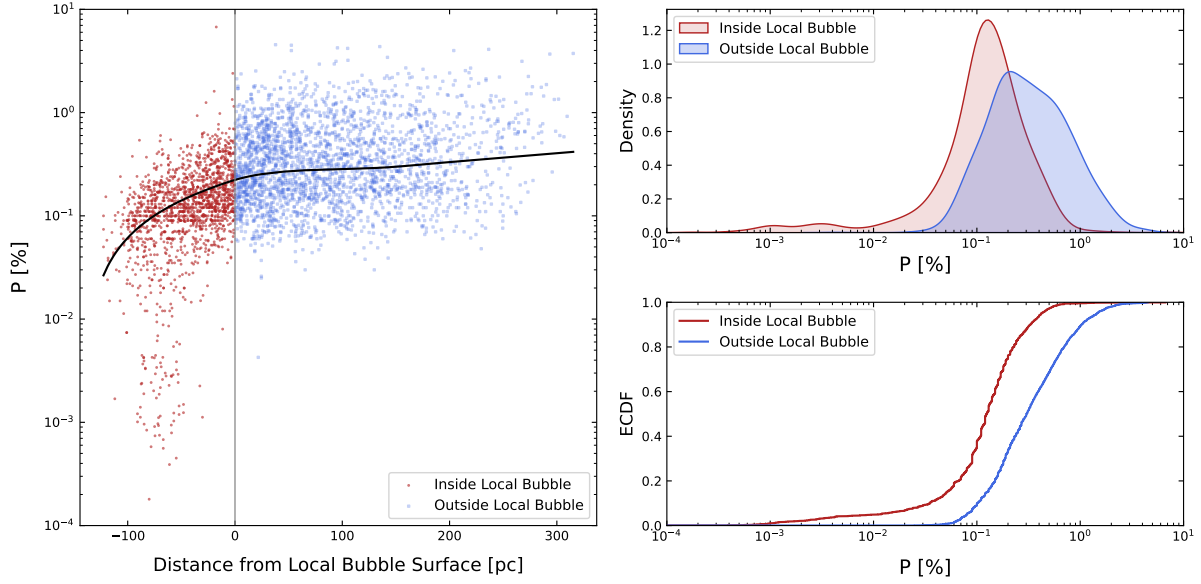


Figure 12: Polarization fraction  $P$  for starlight polarization measurements inside vs. outside of the LB. Left:  $P$  as a function of distance from the nearest surface of the LB. Stars inside the LB are marked by the small red points, while stars outside are marked by the larger and less opaque blue points. The average trend for increasing  $P$  as a function of distance is shown by black curve, generated using LOWESS regression (Locally Weighted Scatterplot Smoothing). Top right: Kernel density estimations of the distributions of inside (red) vs. outside (blue) of the LB. Bottom right: Cumulative distributions of  $P$  for stars inside vs. outside of the LB.

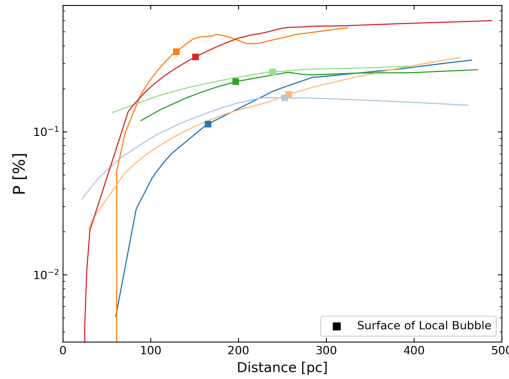


Figure 13: Starlight polarization fraction  $P$  as a function of distance from the Sun for stars along seven random lines of sight, each  $10^0$  in radius. The location of the edge of the LB along each line of sight is marked by a square.

Using PyVista, we calculate the implicit distance between each star and the LB surface and found that  $\sim 37\%$  of the starlight sample falls inside the LB. In Figure 13, we plot  $P$  as a function of distance from the nearest surface of the LB for all stars. A one-sided Kolmogorov-Smirnov (K-S) test suggests that stars inside the LB have significantly lower  $P$  than stars outside the Bubble ( $D=0.43$ ,  $p \ll 0.001$ ), and a moderate trend for increasing  $P$  with distance is present (Spearman  $\rho_s = 0.50$ ,  $p \ll 0.001$ ). This trend is even clearer for

groups of stars along individual lines of sight, as demonstrated in Figure 14 for the average  $P$  as a function of distance from the Sun for seven random lines of sight.  $P$  typically increases rapidly along a given line-of-sight until the surface of the LB is reached, at which point it plateaus. This supports the observed difference in polarization between the interior and exterior of the Bubble identified by (missing citation) and others, with the benefit of the additional precision allowed by the P20 map.

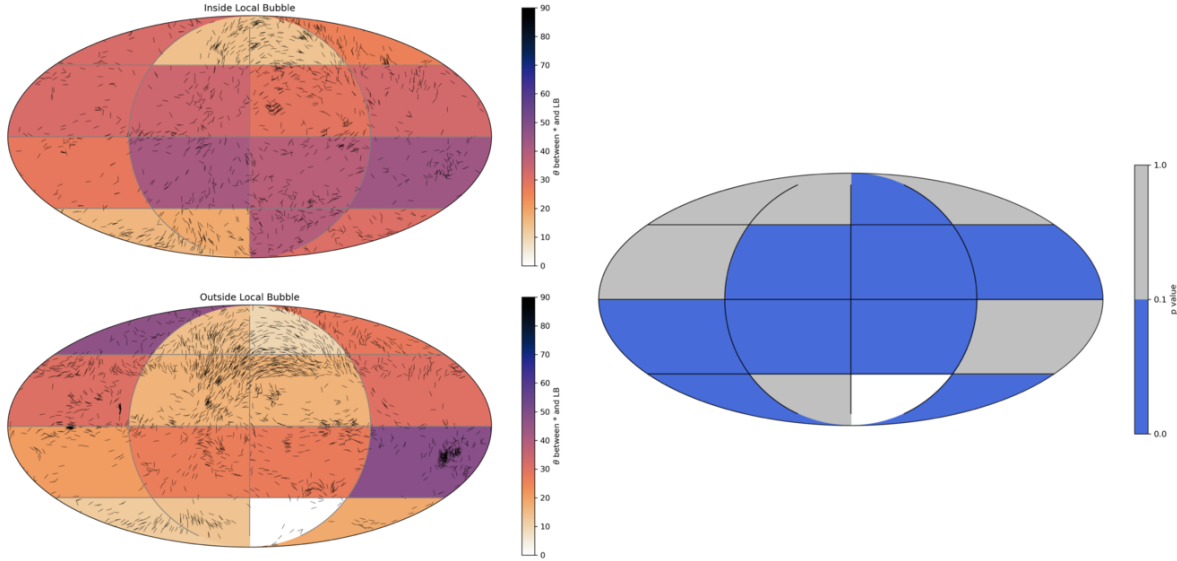


Figure 14: Left: average angle between starlight polarization vectors and the nearby LB B-field for starlight measurements ending inside (top) vs outside (bottom) the LB. Right: Blue cells have K-S test p-values  $\leq 0.10$ , indicating that starlight vectors outside the LB have lower average angle differences than stars inside the LB.

In Figure 12, we compare the orientations of the interior and exterior starlight polarization measurements to our derived B-field over the surface of the LB. The orientation of starlight polarization measurements inside the LB appear to be closer to random with respect to the LB surface field, while starlight polarization measurements outside of the LB mirror the LB’s surface field very closely.

To quantify this behavior, we identify the nearest LB surface points to each star in 2D projection as measured using Haversine distances. We calculate the average absolute dot product between each starlight measurement and its surrounding LB vectors,  $|\vec{\Psi}_* \cdot \vec{\Psi}_\perp|$ , and from this average angle  $\theta$  between the two inferred field types. A K-S test reveals that starlight measurements outside of the LB have significantly higher  $|\vec{\Psi}_* \cdot \vec{\Psi}_\perp|$  than stars inside the LB ( $D=0.15$ ,  $p \ll 0.001$ ).

In Figure 15 we plot the average  $\theta$  for stars inside and outside of the Bubble divided into a uniform grid with cell sizes  $\delta\ell = 90^\circ$ ,  $\delta b = 45^\circ$ . We exclude cells that have fewer than 20 measurements. For each in/out LB cell pair, we perform a one-sided K-S test. If  $p \leq 0.1$ , we conclude that starlight measurements outside the LB are likely to be in closer agreement with the LB surface than interior measurements; this is also shown in Figure 15. We find that exterior measurements are in better agreement over much of the Sky, with the exception of very high latitudes and the cell containing the Orion star-forming region. These analyses suggest that starlight that must pass through the dusty (presumably high polarization) LB shell is more aligned with the Planck-derived LB B-field than starlight that does not need to travel through the shell.

## Conclusions

We have created a 3D map of magnetic field orientation on the surface of the Local Bubble, which is the first 3D visualization of a magnetic field over the surface of an observed superbubble. Our main conclusions are as follows:

- The orientation of the plane-of-sky B-field obtained using Planck dust polarization data appears strongly correlated with features of the LB’s shell.
- Starlight polarization measurements support that the interior of the LB is a low-polarization and B-field strength region, with B-fields inferred from stars inside the shell of the LB being more randomly distributed with respect to the LB surface’s B-field than from stars outside of the shell.

These preliminary results support a strong association between the LB and the B-fields inferred from dust and starlight polarization measurements. Future work will include further quantifying the association between the LB surface and the phenomena described above, and applying our methods to simulated equivalents of the LB.

*Acknowledgements:* The authors acknowledge Interstellar Institute’s program ”With Two Eyes” and the Paris-Saclay University’s Institut Pascal for hosting discussions that nourished the development of the ideas behind this work. We particularly thank Susan Clark, Gina Panopoulou, Laura Fissel, François Boulanger, Jennifer West, Jaime Pineda, Avery Kim, Laura Posch, Olga Borodina, and Cameron Swiggum, for insightful comments. The SAO REU program is funded in part by the National Science Foundation REU and Department of Defense ASSURE programs under NSF Grant no. AST- 2050813, and by the Smithsonian Institution.

*Software:* Astropy (missing citation); (missing citation); CmasHER (missing citation); Glue (missing citation); (missing citation); Healpy (missing citation); Matplotlib (missing citation); Numpy (missing citation); Pandas (missing citation); PyVista (missing citation); scikit-learn (missing citation); [scikit-spatial.readthedocs.io](https://scikit-spatial.readthedocs.io)

## References